Journal of the Mechanics and Physics of Solids 144 (2020) 104102

Contents lists available at ScienceDirect

Journal of the Mechanics and Physics of Solids

journal homepage: www.elsevier.com/locate/jmps

Quantitative spatiotemporal Li profiling using nanoindentation

Luize Scalco de Vasconcelos, Rong Xu, Kejie Zhao*

School of Mechanical Engineering, Purdue University, West Lafayette, IN 47907, USA

ARTICLE INFO

Article history:
Received 5 May 2020
Accepted 28 July 2020
Available online 30 July 2020

Keywords:
Nanoindentation
Diffusion
Amorphous Si
Li-ion battery
Li profiling

ABSTRACT

The rate capability and lifetime of Li-ion batteries is largely dictated by the composition dynamics of the electrodes. We set forth a nanoindentation approach to probe the spatiotemporal Li profile using the functional dependence of the mechanical properties on Li composition. This mechanics-informed material dynamics allows us to measure the composition-dependent diffusivity, assess the rate-limiting process in Li reactions, and quantitatively evaluate the stress regulation on Li transport. The experiments show that Li diffusivity in amorphous Si varies exponentially by three orders of magnitude from the pristine to the fully lithiated state. Lithiation in amorphous Si is limited by diffusion at the micron scale. We further evaluate the thermodynamic driving force for Li diffusion by including the material non-ideality and mechanical stresses. Through computational modeling, we find that the composition dependence of the Li diffusivity in general creates an asymmetry on the rate capability during lithiation versus delithiation. In Si, the exponential dependence results in a fast lithiation that proceeds via a steep concentration gradient compared to a slow and relatively smooth delithiation. This asymmetric behavior appears to be a root cause of Li trapping and loss of the deliverable capacity in Si. This work sheds light on the thermodynamics of Li transport and the lithiation kinetics of amorphous Si. It demonstrates the potential of operando nanoindentation in the mechanics-informed understanding of Li chemistry and aiding battery research beyond mechanical measurement.

1. Introduction

The kinetics of Li reactions plays a decisive role in the rate capability and cyclic life of Li-ion batteries. Charge heterogeneity is a prevalent feature in the composite electrodes (Xu et al., 2019; Yang et al., 2019). The inhomogeneous distribution of Li is associated with issues such as underused and abused regions in the redox active materials and heterogeneous mechanical failure due to the localized strains and damage (McDowell et al., 2012; Xu et al., 2016). The spatiotemporal distribution of Li provides essential information needed to identify the underlying rate-limiting mechanisms and to determine the material properties. The combination of chemical, temporal and spatial measurements on battery materials is a vast challenge because the instrument must be able to probe the sample without exposure to the atmosphere while still accommodating all necessary components to control the reactions and maintaining experimental accuracy.

Advanced techniques with the capability of probing the Li element are under fast development; nonetheless, current solutions still hold many practical limitations and are not easily accessible (Hoffmann et al., 2015; Wolf et al., 2017). Because of the low atomic number, Li detection is challenging and requires ultra-sensitive spectroscopy techniques such as

* Corresponding author.
E-mail address: kjzhao@purdue.edu (K. Zhao).

https://doi.org/10.1016/j.jmps.2020.104102
0022-5096/

electron loss spectroscopy (EELS) (Wang et al., 2011), secondary-ion mass spectrometry (SIMS) (Bordes et al., 2015), and Auger electron spectroscopy (AES) (Radvanyi et al., 2013). Neutron diffraction is sensitive to Li, but the neutron resources are very limited (Mu et al., 2019; Sharma et al., 2010). Hence, most studies rely on indirect measurements to infer the local Li content. For instance, X-ray diffraction (XRD) tomography and atomic force microscopy (AFM) can be used to estimate the composition through local changes in density and volume (Balke et al., 2010; Beaulieu et al., 2003). Optical microscopy and colorimetry are able to estimate the approximate Li content based on the changes in the optical spectrum (Chen et al., 2019; Ghannoum et al., 2016; Harris et al., 2010). One of the most popular approaches is the measurement of lithiation state from the lattice parameters and crystal structures through transmission electron microscopy (TEM) and XRD tomography (Finegan et al., 2019; Lim et al., 2016). A combination of different techniques is also often used to complement the capabilities and correlate different processes taking place at different scales (Pietsch et al., 2016; Wu and Liu, 2018). In this work, we use nanoindentation to probe the spatial distribution of Li over time by making use of the functional dependence of the mechanical properties of elastic modulus and hardness on Li composition (de Vasconcelos et al., 2017). We choose an amorphous Si (a-Si) thin film as a model system.

The incorporation of Si nanoparticles to graphite electrodes in recent years has enabled a 6% improvement in the specific capacity of commercial Li-ion batteries (Mims, 2018). The research aimed at improving the reliability of Si anodes continues to grow worldwide, and pure Si electrodes represent an untapped potential for increasing the cell capacity by 40% (Mims, 2018). A major challenge in Si-dominant anodes (Li et al., 2017; Yu et al., 2015) and other high-energy-density electrodes as well (Beaulieu et al., 2001; Laforge et al., 2008; Xu et al., 2018; Zhang et al., 2019) is the suppression of the mechanical degradation resulting from the inherently large strains associated with lithiation. Information on the kinetic processes associated with Li reactions is crucial to understand and manage mechanical stability as they dictate the buildup of mechanical stresses (Xu and Zhao, 2016).

Despite the commercial interest in Si anodes, the kinetics of Li reactions in a-Si remains unclear. In 2013, two in-situ TEM studies under a large bias voltage (McDowell et al., 2013; Wang et al., 2013) and later a potentiostatic study (Miao and Thompson, 2018) found that the first lithiation of a-Si took place via the propagation of a sharp interface between lithiated and pristine Si, but the following delithiation and cycling proceeded with an evolving, smooth concentration gradient. The sharp interface is a common phenomenon in reactions involving phase transformation; however, Si remains amorphous in these experiments. This observation sparked a debate concerning the underlying rate-limiting process, whether reaction-limited (McDowell et al., 2013; Wang et al., 2013) or diffusion-limited (Miao and Thompson, 2018; Wang et al., 2017), and on the structural changes of amorphous Si upon lithiation (Cubuk and Kaxiras, 2014). Another group compared the rate performance of Si films during lithiation versus delithiation and found that amorphous Si exhibited better rate performance during delithiation, which was attributed to the cut-off voltage being more sensitive to the ohmic polarization during lithiation (Li et al., 2015). In contrast, a few recent studies proposed that the incomplete delithiation by Li trapping is one of the causes of fade in the cyclic efficiency of Si (Lindgren et al., 2019; Rehnlund et al., 2017; Zhu et al., 2019).

The complexity of the Li kinetics in Si and the limitation of existing experimental methods are underscored by another discrepancy in the literature about the Li diffusion coefficient in Si which spans over 8 orders of magnitude (Hü et al., 2018; Simolka et al., 2019; Xie et al., 2010; Yoshimura et al., 2007). It is worth mentioning that electroanalytical techniques such as galvanostatic and potentiostatic intermittent titration (GITT and PITT) are amidst the most popular characterization tools. At the same time, many assumptions of the classical models for GITT and PITT may not uphold in Li-ion applications due to uncertainties arising from parasitic charge injections, varying or not well-defined active surface area (expanding and fracturing surfaces), additional rate-limiting effects (e.g., interfacial reactions), and stress effects on diffusion (Jerliu et al., 2017a; Li et al., 2012; Tripuraneni et al., 2018).

This work sets forth a nanoindentation approach to probe the spatiotemporal Li profile in the electrodes of LIBs. Fig. 1 outlines the structure of the work. The nanoindentation experiments are performed on an a-Si thin film in contact with a Li metal and undergoing chemical lithiation in an argon-filled glovebox (step 1). The outcome of the experiments is the spatial maps of the hardness and elastic modulus of the sample at various lithiation times which spans over several days. The central circle in the sketch represents previous operando nanoindentation measurements of the mechanical properties and the size of lithiated Si upon controlled electrochemical lithiation (de Vasconcelos et al., 2017). The combination of the two experiments yields a spatiotemporal Li concentration map (step 2) that enables the calculation of the apparent diffusivity and tracer diffusivity of Li in Si as a function of the material composition (step 3). The knowledge about the Li distribution and internal stresses in the Si thin film allows a quantitative assessment of stress regulation on Li diffusion. The experimental conditions are simulated using finite element analysis (FEA). The numerical simulations employing a two-way coupling between stress and diffusion validate experimental findings and elaborate the implications on the battery performance (step 4).

This work introduces a new characterization method on Li chemistry using the mechanics tool and provides valuable insights into the kinetic behaviors of battery materials. We find that the diffusion coefficient of Li in a-Si electrodes varies by at least three orders of magnitude with the Li composition. The highly concentration-dependent diffusivity leads to an asymmetrical rate capability and thus an asymmetrical accessible capacity of Si during lithiation versus delithiation. More broadly, this work demonstrates the potential of operando nanoindentation in aiding the research on redox active materials beyond simple mechanical characterization. We present one such application where the local mechanical response is used to inform the local chemical composition. Such an interdisciplinary platform does not only expand the experimental toolbox

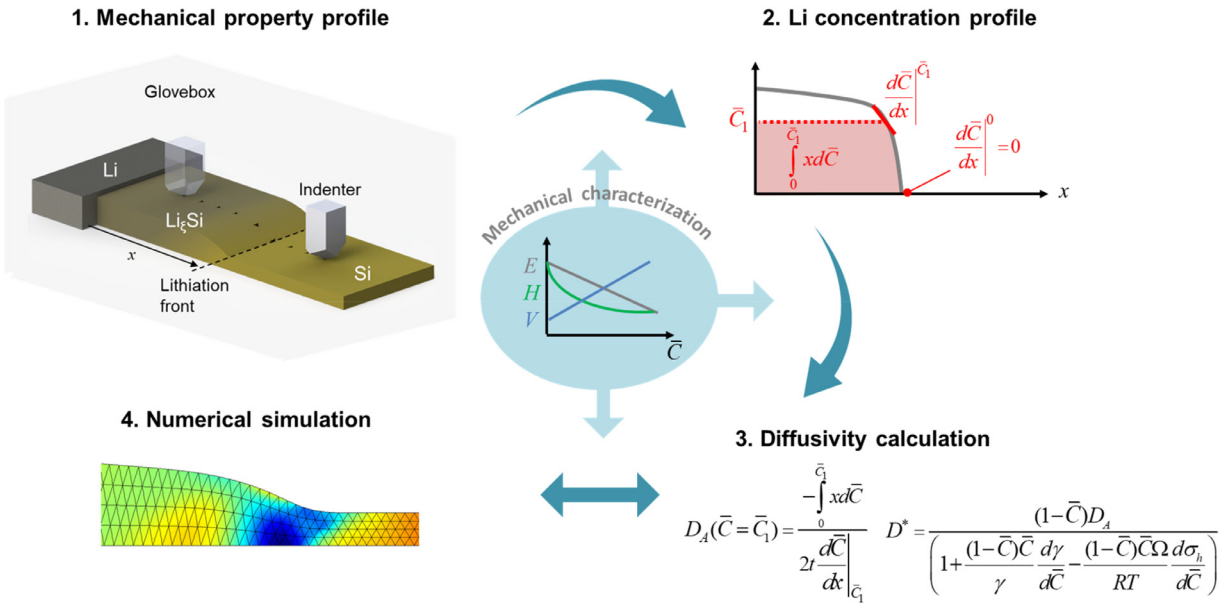

Fig. 1. Nanoindentation experiments for Li profiling in an a-Si thin film enable an examination of the lithiation kinetics and a quantitative study of Li diffusion under stresses. Nanoindentation probes the spatial distribution of the mechanical properties of the thin-film electrode undergoing chemical lithiation in an inert environment (step 1). Li concentration is obtained by converting the mechanical property profiles using their functional dependence on Li composition (step 2). The apparent diffusivity and tracer diffusivity of Li at a given material composition can be determined analytically based on the Li profiles (step 3). Finite element modeling validates the experimental output and evaluates Li transport under concurrent chemical and mechanical driving forces (step 4).

to detect the Li concentration which is difficult to achieve, but also makes it possible to evaluate the competing factors of chemical and mechanical driving forces of Li transport in a quantitative manner.

2. Experimental methods

2.1. Sample preparation

Amorphous Si films are prepared using a Leybold E-beam Evaporator. A 50 nm Ti layer is first deposited onto a 1 mm thick silica substrate, followed by the deposition of a 300 nm copper film, and then by a 500 nm Si film. The deposition rate is 0.5 Å/s in all steps. The amorphous structure of the Si films fabricated by E-beam evaporation under similar conditions has been verified by previous studies (Kugler et al., 1989; Michael et al., 2015). A commercial Li metal ribbon (99.9% purity, Sigma-Aldrich) is used to conduct chemical lithiation of the Si film.

2.2. Nanoindentation

Instrumented nanoindentation (Keysight G200) installed in an argon-filled glovebox (mBraun Labstar) is used to perform two sets of tests: (i) elastic modulus and hardness measurements and (ii) topography profiling. For (i), a Berkovich tip penetrates the sample with an indentation strain rate of 0.05 s^{-1}, until the indentation depth of 250 nm is reached. After a 10 s dwell time, the indenter partially withdraws, and the load is held constant for roughly 60 s to measure and correct the drift due to thermal and chemical effects (de Vasconcelos et al., 2017). The hardness is given by:

$$H = \frac{P}{A}, \tag{1}$$

where the applied load P is prescribed, and the projected contact area A is calculated from the relationship between the tip geometry, tip displacement, and the contact stiffness S (Oliver and Pharr, 2004; Pharr et al., 1992). The elastic modulus of the sample E is calculated by:

$$\frac{1}{E_r} = \frac{1-\nu^2}{E} + \frac{1-\nu_i^2}{E_i}, \tag{2}$$

where the elastic modulus and Poisson's ratio of the diamond tip (E_i, ν_i) are 1141 GPa and 0.07, respectively (Tsui and Pharr, 1999). The Poisson's ratio ν for Si is assumed to be 0.22 (Berla et al., 2015). The reduced elastic modulus E_r is given

by:

$$E_r = \frac{S\sqrt{\pi}}{2\beta\sqrt{A}}, \tag{3}$$

where β is 1.034 for the Berkovich tip (Tsui and Pharr, 1999). The continuous stiffness measurement (CSM) method is employed to measure the contact stiffness S as a function of the tip displacement from the in-phase material response to an oscillating signal superimposed on the semi-static indentation force (Hay et al., 2010). The harmonic displacement and frequency of the superimposed signal are set to be 2 nm and 45 Hz, respectively. Same as in our previous work (de Vasconcelos et al., 2017), the elastic modulus and hardness are extracted at an indentation depth of 80 nm to ensure a direct comparison between the two studies. For the test set (ii), the sample topography is profiled by maintaining the tip in contact with the sample through a small, constant load of 10 μN, while measuring the tip displacement as the stage moves with a velocity of 10 μm/s in the prescribed direction.

3. Theory of coupled diffusion and large elastoplastic deformation

This section outlines the theory of coupled diffusion and large elastoplastic deformation that we use in the finite element modeling of Li insertion in Si. It also describes the methodology that we use to derive the Li diffusivity, including the tracer diffusivity and apparent diffusivity, as a function of the Li composition based on the measured Li profiles. Due to the large specific capacity in the high-energy-density electrodes, the kinetic processes of lithiation and delithiation are strongly coupled with the deformation non-linearity and mechanical stresses. The stresses alter the energy landscape of Li transport and place a significant effect on the charging/discharging kinetics of battery materials. Here we give a brief review of the continuum theory of coupled diffusion and large elastoplastic deformation (Zhao et al., 2011a) to facilitate the discussion of stress regulation on Li diffusion in the computational modeling.

3.1. Kinematics of deformation

The material coordinates in the reference framework, $\mathbf{X}$, translate to the spatial coordinates in the current configuration, $\mathbf{x}$, by the displacement vector, $\mathbf{u}(\mathbf{X}, t)$:

$$\mathbf{x}(\mathbf{X}, t) = \mathbf{X} + \mathbf{u}(\mathbf{X}, t). \tag{4}$$

In the reference configuration, the mechanical equilibrium is enforced by

$$\nabla \cdot (\mathbf{FS}) = 0, \tag{5}$$

where $\nabla \cdot$ indicates the divergence in the reference configuration, $\mathbf{S}$ the second Piola-Kirchoff stress, and $\mathbf{F} = \frac{\partial \mathbf{x}}{\partial \mathbf{X}} = \nabla \mathbf{u} + \mathbf{I}$ is the deformation gradient. The deformation gradient contains elastic and inelastic contributions:

$$\mathbf{F} = \mathbf{F}_{\text{el}}\mathbf{F}_{\text{inel}}. \tag{6}$$

The inelastic contribution includes both the deformation by Li insertion and extraction, and deformation due to plasticity: $\mathbf{F}_{\text{inel}} = \mathbf{F}_{\text{Li}}\mathbf{F}_{\text{pl}}$. The Li induced deformation is assumed to be isotropic:

$$\mathbf{F}_{\text{Li}} = (1 + \Omega C)^{1/3}\mathbf{I}, \tag{7}$$

where Ω is the partial molar volume of Li in the host and C is the molar concentration in the reference configuration. Li induced inelastic volume change per unit reference volume is given by $J_{\text{Li}} = det(\mathbf{F}_{\text{Li}}) > 0$. The plastic deformation accounts for the shape change while keeping the volume constant, $J_{\text{pl}} = det(\mathbf{F}_{\text{pl}}) = 1$. The overall volume change per unit of reference volume is

$$J = \det(\mathbf{F}) > 0. \tag{8}$$

We choose an elastic and perfectly plastic constitutive model. The second Piola-Kirchoff stress is determined by

$$\mathbf{S} = J_{\text{inel}}\mathbf{F}_{\text{inel}}^{-1}(\mathbf{C} : \mathbf{E}_{\text{el}})\mathbf{F}_{\text{inel}}{}^{-\text{T}}, \tag{9}$$

where ":" represents the double contraction between the fourth-order stiffness tensor $\mathbf{C}$ and the second-order elastic Green-Lagrange strain tensor,

$$\mathbf{E}_{\text{el}} = \frac{1}{2}\left(\mathbf{F}_{\text{el}}{}^{\text{T}}\mathbf{F}_{\text{el}} - \mathbf{I}\right). \tag{10}$$

The second Piola-Kirchoff stress $\mathbf{S}$ (reference configuration) relates to the Cauchy stress $\boldsymbol{\sigma}$ (current configuration) as

$$\boldsymbol{\sigma} = J^{-1}\mathbf{FSF}^{\text{T}}. \tag{11}$$

We use the von Mises stress yield criterion for the plastic deformation. The yield function is written as

$$F_y = \sigma_{\text{mises}} - \sigma_y = \sqrt{\frac{3}{2}\boldsymbol{\sigma}_d : \boldsymbol{\sigma}_d} - \sigma_y, \tag{12}$$

where $\boldsymbol{\sigma}_d$ is the deviatoric stress and σ_y is the yield stress. The plastic flow rule follows (Lubliner, 2008):

$$\dot{\mathbf{C}}_{\mathbf{pl}}^{-\mathbf{1}} = -\frac{2\lambda}{J}\mathbf{F}^{-1}\frac{\partial F_y}{\partial \boldsymbol{\sigma}}\mathbf{F}\mathbf{C}_{\mathbf{pl}}^{-1} \tag{13}$$

where $\mathbf{C}_{\mathrm{pl}}^{-1} = \mathbf{F}_{\mathrm{pl}}^{-1}\mathbf{F}_{\mathrm{pl}}^{-\mathrm{T}}$ and $\dot{\mathbf{C}}_{\mathrm{pl}}^{-1} = (\dot{\mathbf{F}}_{\mathrm{pl}}^{-1}\mathbf{F}_{\mathrm{pl}}^{-\mathrm{T}} + \mathbf{F}_{\mathrm{pl}}^{-1}\dot{\mathbf{F}}_{\mathrm{pl}}^{-\mathrm{T}})$. The yield function $F_y$and the plastic multiplier λ fulfill the Kuhn-Tucker conditions:

$$\lambda \geq 0, F_y \leq 0, \lambda F_y = 0. \tag{14}$$

3.2. Kinetics of diffusion

In order to derive the driving forces for diffusion, it is necessary to establish the diffusion mechanism. Si diffusion is several orders of magnitude slower than that of Li (Johari et al., 2011; Wang et al., 2015), and therefore Si is considered to be immobile. For simplicity, and following the previous studies (Bucci et al., 2014; Di Leo et al., 2015), we assume that Li diffusion takes place by hopping through a fixed network of available sites. In this case, the driving force for Li diffusion is the difference between the chemical potential of Li, μ_{Li}, and the chemical potential of the vacant sites, μ_V. This potential difference is called the diffusion potential and it takes the following form (Larché and Cahn, 1985; Verbrugge and Koch, 1996):

$$\Phi = \mu_{Li} - \mu_V = \mu_0 + RT\ln\left(\gamma\frac{\bar{C}}{1-\bar{C}}\right) - \sigma_h\Omega, \tag{15}$$

where μ_0 is a reference potential, R is the gas constant and T is the temperature, and γ is the activity coefficient. The hydrostatic stress is $\sigma_h = tr(\boldsymbol{\sigma})/3$, and $\bar{C}$ is the normalized Li concentration, where $\bar{C} = 1$ corresponds to the fully lithiated state (all available sites for Li are occupied) and $\bar{C} = 0$ corresponds to pure Si. It is worth noting that diffusion in an amorphous network is complex (Balluffi et al., 2005; Cammarata, 2009) and other effects such as some degree of void relaxation and site nucleation could also play a role (Bower et al., 2015; Li et al., 2020).

Li flux in the deformed configuration is given by

$$\mathbf{j} = -\frac{cD^*}{RT}\nabla_x\Phi. \tag{16}$$

where c and ∇_x are the Li concentration and the gradient in the deformed configuration, respectively. $M = D^*/RT$ is the mobility, where the coefficient D^* is known as the tracer diffusivity (Bazant, 2013) or self-diffusivity (Balluffi et al., 2005). Li flux in the undeformed configuration (Xu and Zhao, 2018) can be derived as

$$\mathbf{J} = -\frac{CD^*}{RT}\mathbf{F}^{-1}\mathbf{F}^{-T}\nabla\Phi. \tag{17}$$

The mass conservation is enforced by

$$\frac{\partial C}{\partial t} = -\nabla\cdot\mathbf{J}. \tag{18}$$

3.3. Derivation of diffusivity based on Li profiles

We calculate the diffusion coefficient of Li in lithiated Si ($\mathrm{Li}_\xi\mathrm{Si}$) based on the Li profiles using the Matano-Boltzmann (M-B) approach (Poirier and Geiger, 2018). Here this approach is validated for Li diffusion under stress. In the experiments, the Li metal is placed in direct contact with the a-Si film. At a given time, the spatial Li distribution within the Si film is obtained by measuring the elastic modulus and hardness of lithiated Si and also by scanning the topography of the film. In this setup of chemical lithiation, Li diffusion is approximated as a one-dimensional problem with the concentration varying mostly along the longitudinal direction x as shown in Fig. 1. For now, we neglect the effect of surface diffusion and assume a homogeneous distribution of Li across the film thickness. We will estimate the uncertainty brought by the surface diffusion of Li in a later section. Since the Si film is constrained by the substrate, lithiated Si expands mostly in the direction perpendicular to the substrate, and the deformation along the longitudinal direction is negligible ($x \sim X$). The shear deformation (the off-diagonal terms of $\mathbf{F}$) is also small relative to the thickness change of the film. Eq. (18) can be recast into the one-dimensional form:

$$\frac{\partial\bar{C}}{\partial t} = \frac{\partial}{\partial x}\left(\frac{\bar{C}D^*}{RT}\frac{\partial\Phi}{\partial x}\right) = \frac{\partial}{\partial x}\frac{D^*}{(1-\bar{C})}\left(1 + \frac{(1-\bar{C})\bar{C}}{\gamma}\frac{\partial\gamma}{\partial\bar{C}} - \frac{\Omega(1-\bar{C})\bar{C}}{RT}\frac{\partial\sigma_h}{\partial\bar{C}}\right)\frac{\partial\bar{C}}{\partial x}, \tag{19}$$

where $\bar{C} = C/C_{\max}$ is the normalized concentration in the reference configuration. $C_{\max}$ is the Li concentration in fully lithiated Si, $\mathrm{Li}_{3.75}\mathrm{Si}$ (Hatchard and Dahn, 2004). Here we name the pre-factor to the concentration gradient in Eq. (19) as the apparent diffusivity D_A, such that

$$\frac{\partial\bar{C}}{\partial t} = \frac{\partial}{\partial x}\left(D_A\frac{\partial\bar{C}}{\partial x}\right), \tag{20}$$

where

$$D_A = \frac{D^*}{(1-\bar{C})}\left(1 + \frac{(1-\bar{C})\bar{C}}{\gamma}\frac{\partial \gamma}{\partial \bar{C}} - \frac{\Omega(1-\bar{C})\bar{C}}{RT}\frac{\partial \sigma_h}{\partial \bar{C}}\right). \tag{21}$$

For diffusion in a semi-infinite medium with a constant-concentration boundary condition and the apparent diffusivity being a sole function of the composition, the M-B approach can be readily adopted to determine the diffusivity as a function of the material composition (Boltzmann, 1894; Crank, 1975; Mitra et al., 1991). In the experiments, the Si film is sufficiently long so that lithiation does not reach the opposite end of the film. The timescale of the experiments (several days) is also sufficient to ensure the boundary of Si in direct contact with Li is at the fully lithiated state for the duration of the experiments. If the apparent diffusivity in Eq. (21) can be expressed as a single function of composition,

$$D_A = D_A(\bar{C}, \sigma_h, D^*, \gamma) = D_A(\bar{C}), \tag{22}$$

the Boltzmann transformation using the variable $\lambda \equiv x/t^{1/2}$ will be applicable. Considering that the system is isothermal, the material properties are history independent, and that the stress field can be uniquely determined by the Li composition (more discussions in Section 4.2), Eq. (22) holds and the diffusion kinetics in the set of experiments would be indistinguishable from that of a classical Fick's law. Additional discussions on some special cases where the self-stress (diffusion-induced stress) results in a deviation from Fick's behavior can be found in the literature (Larche and Cahn, 1982).

With the introduction of the Boltzmann variable $\lambda \equiv x/t^{1/2}$, Eq. (20) can be written into an ordinary differential equation:

$$-\frac{\lambda}{2}\frac{d\bar{C}}{d\lambda} = \frac{d}{d\lambda}\left(D_A\frac{d\bar{C}}{d\lambda}\right). \tag{23}$$

In the experiment, the concentration is expected to saturate quickly and remain fixed at the boundary with the Li metal, $\bar{C}(x=0, t>0) = \bar{C}(\lambda = 0) = C_S$, and the film is sufficiently long that it can be assumed to be semi-infinite, $\bar{C}(x = +\infty, t>0) = \bar{C}(\lambda = +\infty) = 0$. Integrating Eq. (23) from $\lambda = +\infty$ to $\lambda = x/\sqrt{t}$, and knowing that $D\frac{d\bar{C}}{d\lambda} = 0$ when $\bar{C} = 0$, it gives (Crank, 1975; Okugawa and Numakura, 2015):

$$D_A(\bar{C} = \bar{C}_1) = \frac{-\frac{1}{2t}\int_0^{\bar{C}_1} x d\bar{C}}{\left(\frac{d\bar{C}}{dx}\right)\Big|_{\bar{C}_1}}. \tag{24}$$

While the apparent diffusivity D_A can be calculated directly from the Li profile, the tracer diffusivity D^* requires knowledge about the evolving stress field and the material non-ideality. Following the previous work (Verbrugge and Koch, 1996; Wohl, 1946), the activity coefficient γ is derived by assuming that the excess free energy can be modeled as a series expansion in $\bar{C}$:

$$RT\ln(\gamma) = \sum_{k=2}^{N}\Omega_k k\bar{C}^{k-1}, \tag{25}$$

where Ω_k are a set of self-interaction coefficients. In this work, we use the self-interaction coefficients for $Li_\xi Si$ ($0 \le \xi \le 3.75$) which were fit to the open-circuit potential data in first-principles modeling (Bucci et al., 2014; Chevrier and Dahn, 2009). The estimation of the hydrostatic stress within the lithiated Si will be discussed in detail in Section 4.2.

3.4. Finite element implementation

We use finite element modeling to simulate the concurrent diffusion and stresses in the Si thin film upon chemical lithiation and demonstrate the implications of the experimental output on the battery performance. The weak formulations of the deformation kinematics and the diffusion kinetics can be found in a previous work (Xu and Zhao, 2016). The specific conditions relevant to the current study will be explicitly stated. The multiphysics time-dependent solver MUMPS (Multifrontal Massively Parallel sparse direct Solver) in COMSOL is used to solve the co-evolution of the concentration and stress fields. The order and shape of the test functions for the diffusion potential $\Phi(\mathbf{X}, t)$ and displacement $u(\mathbf{X}, t)$ are quadratic Lagrange and cubic Lagrange, respectively.

4. Results

We adopt a nanoindentation approach to quantitatively measure the composition gradient in a material by means of its known mechanical properties. A model system consists of an a-Si film laterally in contact with a Li metal ribbon (schematic in Fig. 1, step 1). Chemical lithiation proceeds spontaneously from the Li metal side towards the other end of the Si film. The test is conducted in an argon-filled environment with the H_2O and O_2 levels below 0.5 ppm. Optical microscopy images on the top surface of the film show that the lithiation process is marked by a sharp color contrast, roughly in parallel to the Li|Si contact, which propagates over time. The supplementary video shows the moving lithiation front. The sharp

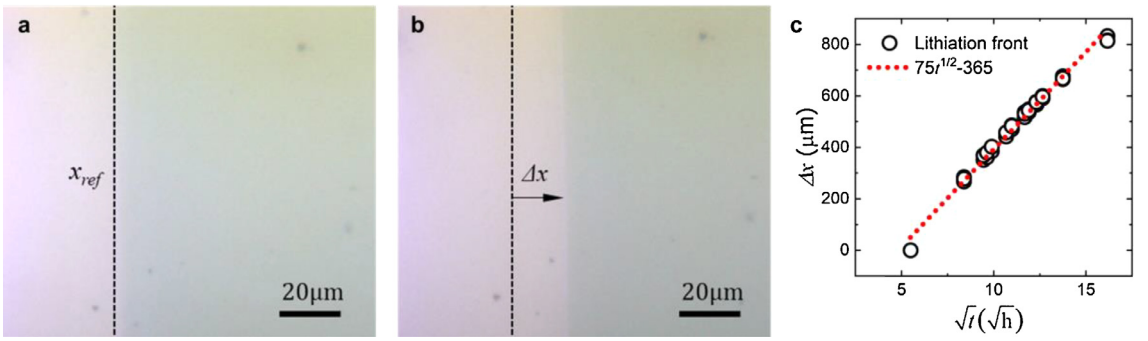

Fig. 2. Optical images of the moving lithiation front in an amorphous Si thin film upon Li reaction at (a) a reference time and (b) an elapsed time Δt. (c) Measurement of the moving front at three separate locations for each given time (circles) and the linear fitting (dotted line). The constant slope between Δx and $\sqrt{t}$ indicates diffusion-limited kinetics of lithiation in the amorphous Si thin film.

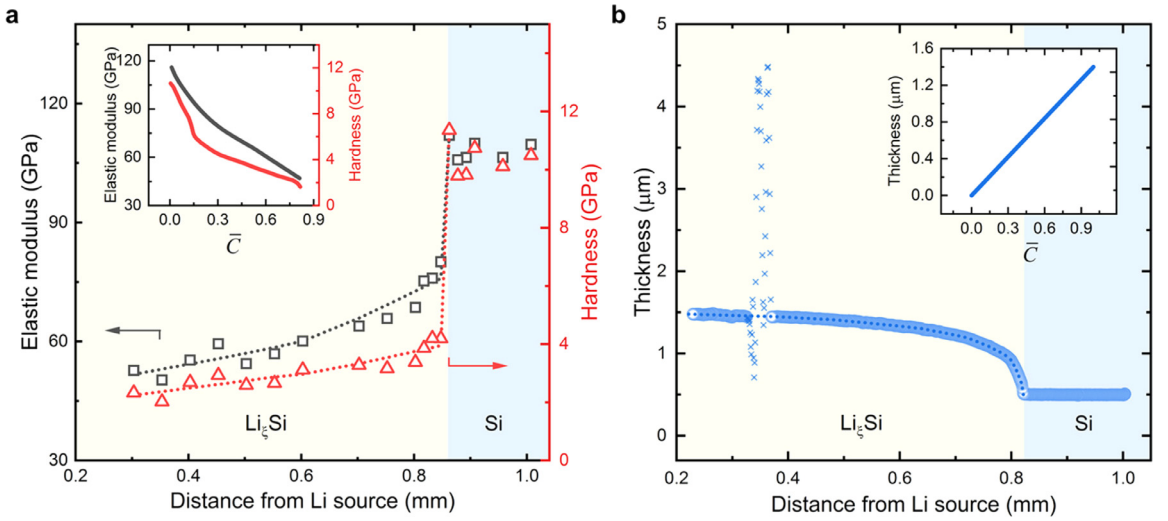

Fig. 3. Spatial distributions of (a) the elastic modulus and hardness, and (b) film thickness along the Li propagation direction. The insets show the elastic modulus, hardness, and film thickness as a function of the Li concentration in Si (de Vasconcelos et al., 2017). The inset functions convert the mechanical measurements to the Li profiles.

contrast corresponds to the interface between lithiated and pristine Si. The dark spots behind the Li front are blisters/defects generated by the Li sweeping through the Si film. We track the position of the lithiation front starting from a reference position x_{ref} at $t = 30$ h, Fig. 2a and 2b. $t = 0$ h corresponds to the time at which the Li metal is placed in contact with the Si film. Fig. 2c plots the displacement of the moving front Δx as a function of $\sqrt{t}$. The position of the lithiation front is measured at three separate locations for each given time. The dotted line shows a linear fitting of the experimental results. The constant slope between Δx and $\sqrt{t}$ is a strong indication of diffusion-limited kinetics of lithiation in the amorphous Si thin film. This result is different from the observation of previous TEM studies that the first lithiation of a-Si proceeds via a two-phase and two-step mechanism (McDowell et al., 2013; Wang et al., 2013). Such discrepancy is likely due to the very different time scales in the experiments (i. e., seconds in TEM characterizations versus tens of days in this measurement) and also possibly caused by different experimental conditions (i. e., a large bias voltage applied in TEM experiments versus chemical lithiation without an applied voltage in the current work). An earlier study by Wang et al. noted this difference in the mechanistic understanding of lithiation in a-Si and concluded that Li reaction in a-Si at a conventional charging rate proceeds via single phase kinetics (Wang et al., 2017).

4.1. Li profiling and apparent diffusivity

We track the spatial distribution of the hardness and elastic modulus over time in the lithiated Si thin film by performing multiple arrays of indentations along the lithiation direction. Fig. 3a shows an example of the elastic modulus (black squares) and hardness (red triangles) as a function of the distance from the Li source at the time $t = 150$ h. The inset plot is reproduced from our previous operando nanoindentation experiment (de Vasconcelos et al., 2017) and shows the dependence of the elastic modulus and hardness on the Li concentration in Si, where $\bar{C} = 0$ corresponds to pure Si and $\bar{C} = 1$ to

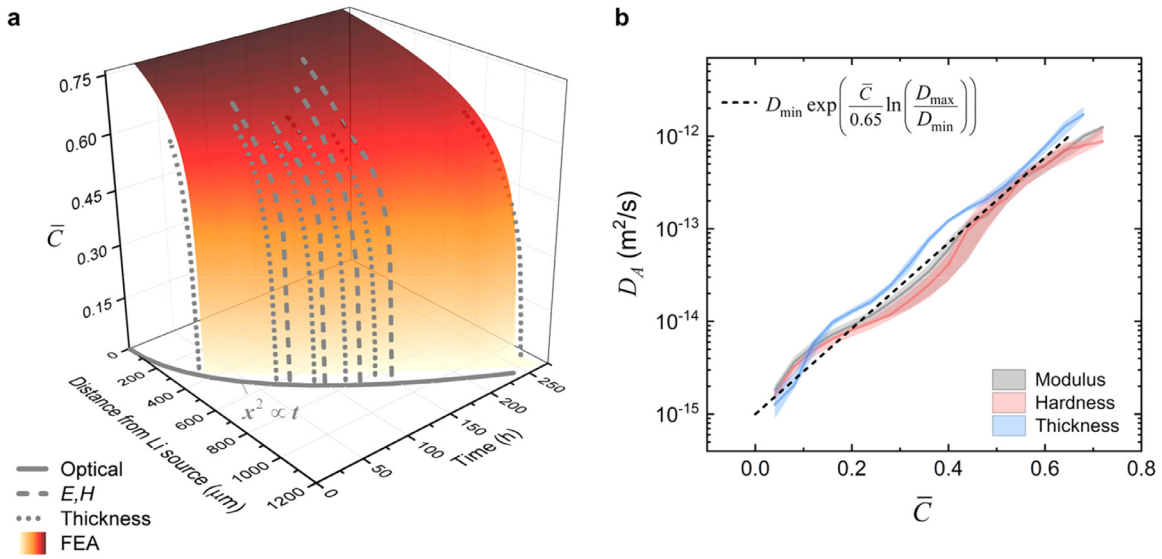

Fig. 4. (a) The spatiotemporal distribution of Li concentration. The gray lines show the results from the nanoindentation measurements of the elastic modulus and hardness (dashed lines), the thickness profiles (dotted line), and the optical imaging of the moving lithiation front (solid line). The contour plot shows the FEA results. (b) The apparent Li diffusivity as a function of the Li composition determined by the experimental results in (a). The experimental conditions are simulated in FEA using the exponential diffusivity function shown by the dashed line in (b). The numerical results of the Li profile are contour plotted in (a) to compare with experiments.

fully lithiated Si ($Li_{3.75}Si$). The load-displacement curves, as well as the complete elastic modulus and hardness data as a function of the indentation depth for the nanoindentation array in Fig. 3a is shown in the Supplementary Figure S1. Combining the spatial distribution of the mechanical properties and their one-to-one relationship with the Li concentration, Li profiles in the a-Si thin film can be mapped. For instance, the elastic modulus and hardness ahead of the lithiation front (light blue regimes in Fig. 3) are roughly 110 GPa and 10 GPa, respectively, which correspond to the properties of pristine Si. Closer to the Li metal, the elastic modulus is 50 GPa and hardness is 2 GPa, which indicates a Li composition of $\bar{C} \sim 0.75$, or $Li_{2.8}Si$. In addition, we take advantage of the volumetric expansion of Si upon Li insertion to determine the local material composition based on the known relationship between the volumetric strain and the Li content (Yoon et al., 2016). Fig. 3b shows the thickness profile of the film at the time $t = 143$ h. The spike marked by cross-symbols represents a type of whisker that grows during lithiation out of the pre-existing blisters from the deposition process (supplementary video). These spikes are discarded in our analysis. The dashed lines in Figs. 3a and 3b show the filtered and smoothed data used to compute the Li concentration.

Following the spatial scanning of the mechanical properties and the topology of the amorphous thin film at different times, the spatiotemporal concentration of Li is determined and shown in Fig. 4a. A total of 10 test batches are conducted at different times in the course of 11 days, alternating between topography and mechanical properties measurements. For each batch, the sample is profiled at three separate positions across the width of the sample (near each edge and at the center perpendicular to the moving front direction) to verify that the results are independent of the choice of the measured location. Supplementary Figure S2 shows the complete dataset of the Li concentration profiles measured through the mechanical properties and film thickness measurements. The averaged Li profiles in the two sets of experiments are depicted by the dashed and dotted lines, respectively, in Fig. 4a. The position of the moving lithiation front determined from the optical imaging (dashed line in Fig. 2c) is reproduced in Fig. 4a (continuous line) to complement the nanoindentation data.

For each Li concentration profile measured at a given time, we calculate the apparent Li diffusivity D_A using Eq. (24). Note that D_A represents the proportionality coefficient between the gradient of Li concentration and the Li flux in Eq. (20), and it does not differentiate the mechanical and chemical driving forces for Li diffusion. The solid gray, pink, and blue lines in Fig. 4b show the median apparent diffusivities calculated from the Li profiles through the modulus, hardness, and thickness measurements, respectively, while the shadowed areas indicate the range between the 25% and 75% percentiles. The dashed line in Fig. 4b shows that an exponential form $D_A = D_{\min} \exp(\frac{\bar{C}}{0.65} \ln(\frac{D_{\max}}{D_{\min}}))$ with $D_{\max} = 1 \times (10^{-12}) \mathrm{m}^2/\mathrm{s}$ and $D_{\min} = 1 \times (10^{-15})$ m^2/s matches well with the experimental data. This exponential form of Li diffusivity explains the steep concentration gradient observed by the optical microscope – the slow diffusion of Li in the pristine Si (as compared to lithiated Si) acts as a bottleneck for Li flux and causes the accumulation of Li at the lithiation front. Indeed, prior theoretical and experimental studies reported that Li diffusivity in amorphous Si was higher in the lithiated state than in the pristine state (Chou and Hwang, 2013; Hü et al., 2018; Miao and Thompson, 2018; Sivonxay et al., 2020; Wang et al., 2015; Xie et al., 2010). Nevertheless, the shape and magnitude of the Li diffusivity vary widely across the literature. We will discuss the literature results in more detail in Section 4.3.

The colored contour plot in Fig. 4a shows the concentration profile through the finite element modeling using $\frac{\partial \bar{C}}{\partial t} = \frac{\partial}{\partial X} D_A \frac{\partial \bar{C}}{\partial X}$ as the governing equation and the measured apparent diffusivity as the input parameter. This phenomenological equation does not distinguish the specific driving force for Li diffusion; instead, both the chemical and mechanical effects in the diffusion potential are embedded in the experimental value of the apparent diffusivity D_A. We note that Li concentration in the experiments is not measured all the way up to $x = 0$ to prevent collision of the tip with the Li metal; hence, the equilibrium concentration C_S at the boundary where Si is in contact with Li is not directly measured. It is possible that the equilibrium concentration at the boundary of the Li-Si contact does not reach the theoretical maximum value ($\bar{C}_S < 1$) due to the stress effect. We will show that this equilibrium concentration is approximately $\bar{C}_S \sim 0.8$ in a later section. In the finite element modeling, we assume that the exponential form of the apparent diffusivity D_A can be extrapolated to higher concentrations. The contour plot in Fig. 4a shows that the numerical result with the concentration $\bar{C}_S = 0.76$ at the boundary matches well the experimental profiles. This comparison demonstrates that the solution of a simple Fick's equation is sufficient to reproduce the experimental output reasonably well. The Fickian diffusion here does not exclude the stress effects on diffusion. If the stress significantly alters the diffusion potential, the result indicates that the hydrostatic stress depends solely on the Li concentration (Larche and Cahn, 1982; Larché and Voorhees, 1996). Next, we will quantify the stress modulation on Li diffusion based on the Li profiles and the relatively simple internal stresses in the a-Si thin film.

4.2. Assessment of stress effect on diffusion

Mechanical stresses alter the rate of diffusion by altering the following factors (Larché and Voorhees, 1996; Philibert, 1996): (i) the diffusion potential, (ii) the equilibrium concentration at the boundary condition, and (iii) the activation energy barrier for diffusion. As discussed in Sections 3.3 and 4.1, the effect (ii) does not interfere with the diffusivity measurement as long as the time needed for the boundary concentration to reach equilibrium is considerably shorter than the duration of the experiment. It is worth noting that the effect (iii) alters Li flux even if the stress field is uniform, whereas the effect (i) impacts the Li distribution only by the presence of a stress gradient. The stress sensitivity of the activation barrier for diffusion in amorphous materials is generally small (Balluffi et al., 2005; Mehrer, 1996). More specifically, for Li diffusion in amorphous Si, two earlier studies evaluated the stress effect via ab-initio molecular dynamics (Ding et al., 2017; Pan et al., 2015). Both studies found that the difference of the tracer diffusivity under a homogeneous 1 GPa compressive stress versus the stress-free tracer diffusivity is less than 10%. This difference is small compared to the drastic change of the Li diffusivity with the composition (over three orders of magnitude), and therefore this effect is neglected in this work.

The diffusion potential in Eq. (15) accounts for both the solution non-ideality and the mechanical driving force, which are used to establish the tracer diffusivity in Eq. (21). Here we adopt the activity coefficient of lithiated a-Si from a prior study (Bucci et al., 2014). The activity coefficient γ was obtained from DFT calculations of the open-circuit potential, as discussed in Section 3.3, and it is a strong function of the Li concentration. To decouple the effects of the mechanical stress and the material non-ideality on Li diffusion, we construct a 2D plane-strain thin film model with symmetric displacement boundary conditions applied on the left and right edges of the sample, traction-free top surface, and stiff spring foundation on the bottom surface. The spring foundation allows a small degree of deformation in the x-direction ($<0.1\ \mu m$) which helps numerical convergence, and it is reasonable given that the Cu and Ti buffer layers below the Si film in the experiment may deform slightly. The initial concentration is zero everywhere except for the left edge where a fixed concentration boundary condition of $\bar{C} = 0.76$ is prescribed to mimic the contact with the Li metal. Li flux is determined by the equation $\mathbf{J} = -D_A \mathbf{F}^{-1}\mathbf{F}^{-T}\nabla \bar{C}$. The thickness of the model is the same as in the experiment, and the length is sufficiently large such that the lithiation front does not reach the opposite edge. Lithiation induced volumetric expansion is described by Eq. (7) where $\Omega = 2.8/C_{\max}$ (Yoon et al., 2016). The theoretical maximum concentration $C_{\max}$ corresponds to $Li_{3.75}Si$ (Chevrier and Dahn, 2009). We use the elastic and perfectly plastic constitutive law to describe lithiated Si. The elastic modulus $E = -80\bar{C} + 120$ GPa and the yield stress $Y \cong \frac{H}{3.5} = -3.15\Theta_{Li} + 3$ GPa are adopted from the nanoindentation measurements (de Vasconcelos et al., 2017), where $\Theta_{Li} = \frac{\xi}{1+\xi}$ is the atomic fraction of Li in $Li_\xi Si$. The proportionality factor of 3.5 between the hardness and the yield stress is an approximation (Tabor, 2000). For metallic glasses, this factor typically ranges from 2.7 to 3.7 (Zhang et al., 2006). Supplementary Figure S3 shows that the yield stress function Y from the nanoindentation experiments is within the range of literature values (Cui et al., 2012; Nadimpalli et al., 2013; Pharr et al., 2013; Sethuraman et al., 2010; Zhao et al., 2012).

Fig. 5a plots the hydrostatic stress at the top (gray lines) and bottom (black lines) surfaces of the film at the times $t = 1$ h (dotted lines) and $t = 20$ h (solid lines). The inset shows the stress profiles within a 10 μm section near the lithiation front. At $t = 1$ h, the hydrostatic stress varies at the top and bottom surfaces and is not uniquely determined by the Li concentration. At $t = 20$ h, the hydrostatic stress in the thickness direction reaches a steady-state and the film is mostly in a state of biaxial stress. The compressive stress increases sharply at low Li concentration and then is capped by the yield strength of the film. The computational result of the hydrostatic stress in the plastic regime agrees well with the biaxial stress state $\sigma_h = -\frac{2}{3}Y$ (dashed red line in Fig. 5a).

With the Li concentration, the stress field, and the thermodynamic activity coefficient determined, we are able to decouple the effects of the mechanical stress and the solution non-ideality on the apparent diffusivity. Fig. 5b shows the correction factor due to the gradient of the hydrostatic stress and the gradient of the activity coefficient with respect to the Li concentration (inset equation of Fig. 5c). For the stress effect, because the thin film deforms mostly within the plastic regime and the yield stress decreases as the concentration increases, $\frac{dY}{d\bar{C}} < 0 \rightarrow \frac{d\sigma_h}{d\bar{C}} > 0$, Eq. (21) shows that the

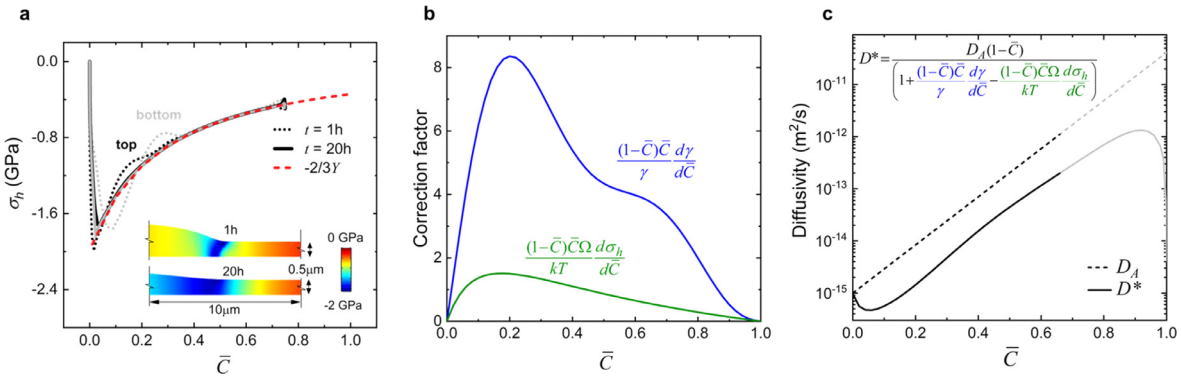

Fig. 5. (a) Computational results of the hydrostatic stress on the top and bottom surfaces of a Si thin film at two lithiation times $t = 1$ h and $t = 20$ h. The hydrostatic stress in the plastic regime matches well with 2/3 of the composition-dependent yield stress. (b) Contributions of the chemical (blue line) and mechanical (green line) driving forces in deriving the Li tracer diffusivity. (c) The apparent Li diffusivity and Li tracer diffusivity as a function of the Li concentration.

hydrostatic stress in the Si thin film minimizes the apparent diffusivity of Li. In other words, the mechanical stress in the Si thin film hinders Li insertion as compared to a stress-free film. This effect is opposite when the thin film deforms within the elastic regime and the magnitude of the compressive stress increases with the Li composition, leading to a negative $\frac{d\sigma_h}{d\bar{C}}$ that accelerates Li insertion. The comparison of the correction factor due to the solution non-ideality and the mechanical stress in Fig. 5b shows the fact that, if Si had been treated as an ideal solution, $\frac{(1-\bar{C})\bar{C}}{\gamma}\frac{d\gamma}{d\bar{C}} = 0$, the stress term in the apparent diffusivity would lead to a negative tracer diffusivity D^* because $\frac{(1-\bar{C})\bar{C}\Omega}{RT}\frac{d\sigma_h}{d\bar{C}}$ is larger than 1 in the concentration range of $\bar{C} = 0.1 \sim 0.4$. This scenario violates the Onsager's symmetry law which is necessary to ensure a positive generation of entropy (Balluffi et al., 2005). Given the dominant effect of the material non-ideality, it is crucial to consider the stress effect on diffusion relative to the chemical driving force. This observation is in agreement with an earlier analysis (Sheldon et al., 2012) which determined that an ideal solution model for lithiated Si leads to an overestimation of the compositional change induced by mechanical stresses. Here we show that the solution non-ideality is more significant on Li transport in the Si thin film. Nevertheless, this conclusion is derived based on the biaxial stress state in the thin film. In another example of a spherical Si particle, we will show that the stress plays an important role in regulating the diffusion kinetics of Li. Fig. 5c is the plot of the apparent diffusivity (dashed line) and the tracer diffusivity (solid line) of Li. The data beyond $\bar{C} = 0.76$ are a mathematical extrapolation. The difference between the tracer and apparent diffusivities of about one order of magnitude is largely due to the thermodynamic activity coefficient as shown in Fig. 5b. Again, the apparent diffusivity is not an intrinsic material property and it depends on the stress state of the host upon Li reactions. There are cases in which the stress effect is substantial on Li diffusion. Here we design another experiment using the Si thin film to further examine the intimate coupling between the stress and Li transport.

We isolate the lithiated Si film from the Li source and monitor the redistribution of Li in the sample due to the presence of the concentration gradient and the stress field. We scratch the film end-to-end across the width direction and separate the major portion of the lithiated film from contacting with the Li metal. The sample surface is cleaned with a cotton swab to remove the scratch debris. We conduct the same spatial scanning of the film topography on both sides of the scratch using nanoindentation and determine the Li profiles in the two sections. Fig. 6a shows the resulting Li redistribution over the course of 67 days following the scratch. The left y-axis shows the film thickness, while the right y-axis shows the corresponding Li concentration using the linear relationship between the film volume and Li concentration. The x-axis is the distance from the edge of the scratch. The left side of the film which is still in contact with the Li metal quickly saturates, reaching the equilibrium Li concentration $\bar{C}_S \sim 0.8$ which is consistent with the computational result in Fig. 4a. In comparison, the Li profile in the film on the right side of the scratch (separated from the Li metal) slowly evolves. The sharp spikes in the thickness profile due to the fabricated scratch and the naturally formed whiskers are displayed in a lighter color (dashed line) and they are excluded from the data analysis. Another note is that during the cleaning some whiskers are knocked off, leaving behind holes of roughly the same diameter. Hence, it seems that the original blisters formed in the deposition process (from which the whiskers grow) are likely hollow inside. Back to the general feature of the Li profile during the self-redistribution, a clear kink forms at the original site of the moving lithiation front. This feature cannot be explained by the concentration gradient of Li which by itself would cause a self-similar Li profile over time. The kink at the lithiation front when Li starts redistributing is a characteristic of the stress-regulated Li diffusion. To quantitatively understand the role of stress, we conduct numerical modeling of Li redistribution in the film using the stress-coupled formulation described in Section 3.

The model geometry is equivalent to the sample. The same constitutive law and material parameters in Fig. 5 are used here for the modeling. To focus on the effect of the biaxial stress state in the thin film and eliminate the effect of deformation non-linearity, we simplify the boundary condition by applying a symmetric condition at the top and bottom surfaces

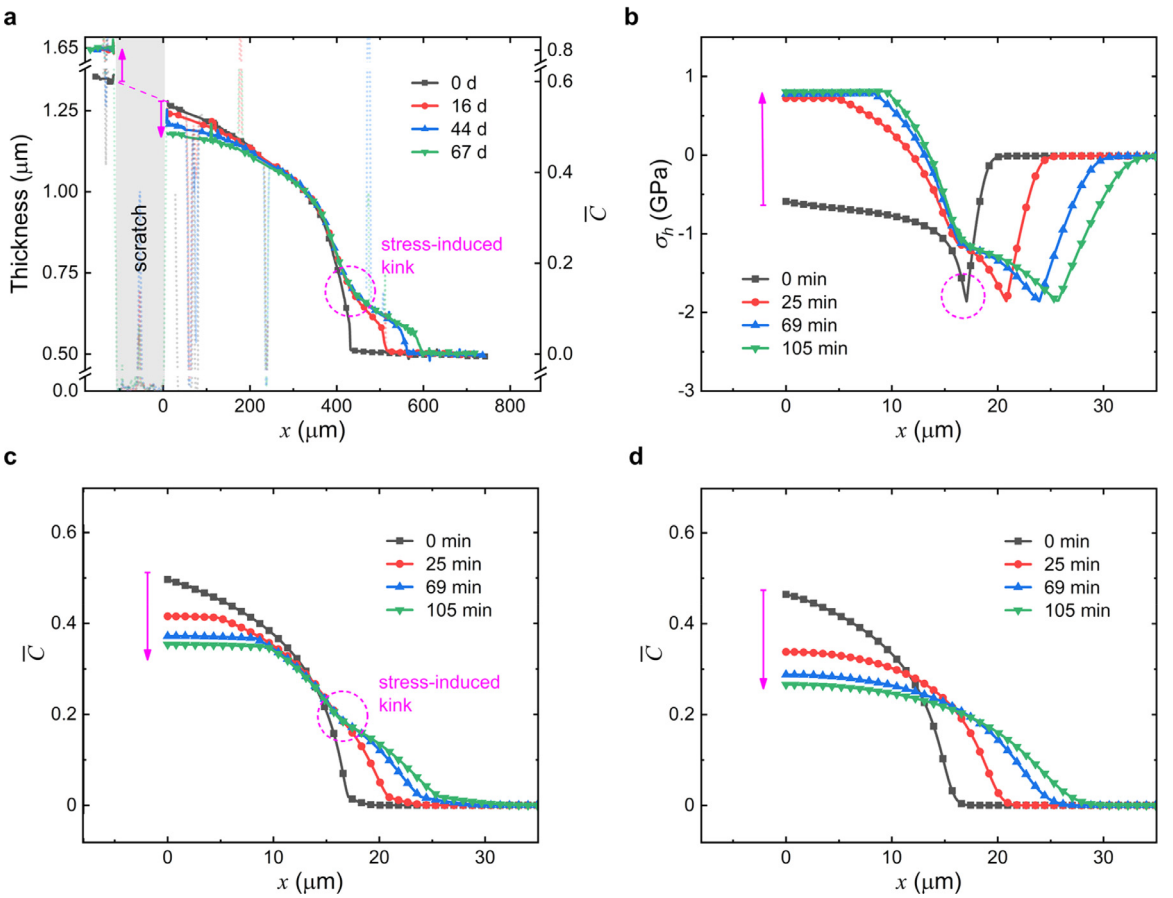

Fig. 6. (a) Experimental results of Li redistribution in Si in the absence of Li influx for over two months. The scratch separates a section of the Si film from the Li metal. The kink in the Li profiles is a characteristic of the stress-regulated Li diffusion. The dashed lines denote material defects in the film. (b) Simulation results of the hydrostatic stress along the Li propagation direction at different times. A drastic change of stress is incurred at the moving lithiation front. (c) and (d) show the simulation results of Li profiles with and without considering the stress effect on Li diffusion, respectively. The self-similarity of the Li profile in (d) is broken because of the Li redistribution (delithiation in the initially lithiated regime and lithiation in the pristine regime) which changes the stress profile over time in (b). The dynamics of mechanical stresses regulate Li flux and induces the kink in Li distribution.

of the film while allowing the in-plane expansion. This simulation condition imposes a biaxial stress state in the film and greatly improves the numerical convergence. The deformation gradient in the longitudinal direction is eliminated in the diffusion equation which mimics the constraint by the substrate to the in-plane deformation of the film. The film is lithiated for a certain time by applying an increasing flux at one end, which is subsequently halted to simulate the scratch of the film and separation from the Li source in the experiment. The concentration redistribution following the separation is monitored. The goal of this modeling is not to replicate the long-time scale and the relatively large size in the experiments, but it is to demonstrate how the mechanical stress modulates Li transport in the thin film. Hence, the time scale in the computation is much shorter than that of the experiment.

Figs. 6b shows the hydrostatic stress in the longitudinal direction of the film along which the Li front propagates, and Fig. 6c shows the Li concentration profiles. The different curves denote the time evolution of the stress and concentration profiles after the removal of the influx boundary condition at $t = 0$ min. Regarding the hydrostatic stress field, two features are noteworthy. First, at any given time, for instance in the stress profile at $t = 0$ min (gray curve, Fig. 6b), there is a peak in the compressive stress near the reaction front (indicated by the dashed pink circle) marking the transition between the elastic and plastic regimes. This local stress field causes major stress gradient near the lithiation front over a range of a couple of micrometers. The second factor is the time evolution of the hydrostatic stress in the initially lithiated regime (behind the lithiation front). The compressive stress in the regime near the scratch eventually switches to a tensile stress (the change is indicated by the pink arrow, Fig. 6b) when the lithiation front advances. This is because the Li extraction from the originally lithiated region causes elastic unloading of the stress followed by plastic yielding of the film with a tensile biaxial stress state. The evolution of the stress field in a thin film during the lithiation and delithiation cycle was analyzed in our earlier work (Zhao et al., 2011b). The simulated Li profiles in Fig. 6c display the same features as observed in the experiments – the Li concentration in the lithiated region gradually decreases over time, Li slowly proceeds to the unreacted

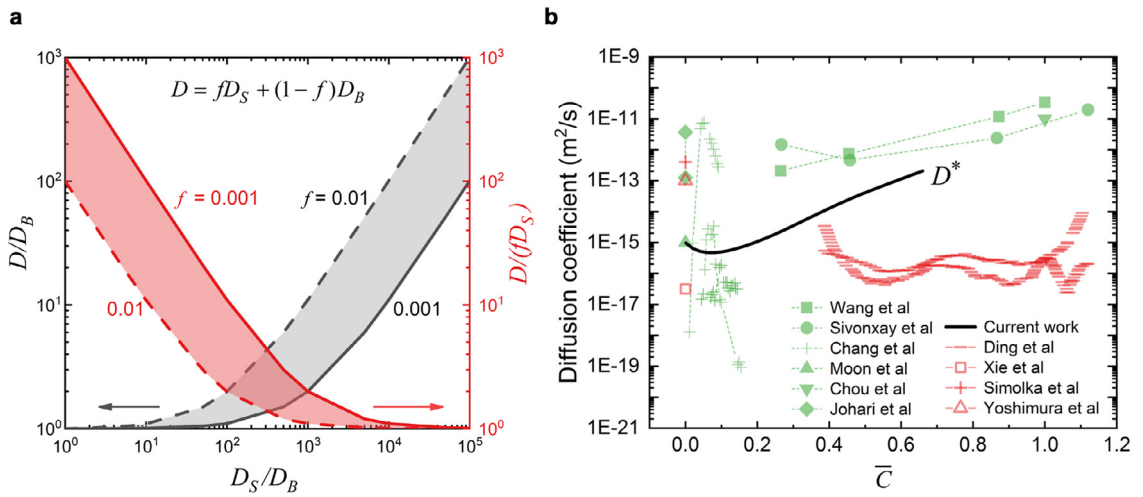

Fig. 7. (a) Uncertainty of the measured Li diffusivity in terms of the ratio between the surface and bulk diffusivities and the fraction of the surface-dominated diffusion. (b) Survey of the composition-dependent Li diffusivity in a-Si. The red symbols represent the experimental measurements. The green symbols are theoretical calculations. The black line denotes the current work.

region of the film, and more importantly, a concave curvature in the Li profile forms nearby the lithiation front (indicated by the pink dashed circle). This curvature forms because the tensile stress developed in the region undergoing delithiation raises the mechanical factor in the diffusion potential that counteracts the chemical driving force from the concentration gradient and acts against the forward Li flux. For comparison, Fig. 6d shows the Li profile upon self-redistribution if the stress term is not included in the diffusion potential. Without the stress regulation, the Li distribution maintains the self-similarity in the profile and the kink observed in the experiments is absent.

4.3. Uncertainty of experiments due to surface diffusion

It is important to recognize the size effect on the diffusion kinetics in the experiments given that the initial film thickness is only 500 nm. The influence of preferential diffusion along a boundary was considered by L. G. Harrison (Harrison, 1961). It is expected that after a sufficiently long time the macroscopic behavior of the diffusive species will obey Fick's law. The measured diffusivity D is a combination of the diffusion coefficients of the bulk D_B and of the surface D_S: $D = fD_S + (1-f)D_B$ (Balluffi et al., 2005), where f is the ratio between the surface diffusion volume and the total volume. Taking the surface diffusion domain to be several interatomic spacings (0.5~5 Å in Si) thick (Ghassemi et al., 2011), and knowing that the film thickness is initially 500 nm, $f = 10^{-2} \sim 10^{-3}$ for $0.5/500 < f < 5/500$. In this calculation, the measured diffusivity will be on the same order of magnitude as the bulk diffusivity if $D_S/D_B < 10^4$. For even larger ratios of D_S/D_B, the nanoindentation measurements can result in an overestimation of the bulk diffusivity. For easier visualization, Fig. 7a shows the D/D_B (left y-axis) and $D/(fD_S)$ (right y-axis) as a function of D_S/D_B. The D/D_B values within the upper bound $f = 0.01$ and the lower bound $f = 0.001$ are shown in the shaded areas. A previous work using density-functional-theory based molecular dynamics simulations showed that the surface diffusivity of Li is only a couple of factors higher than its bulk diffusivity in a-Si (Chou and Hwang, 2013), which would have a close-to-zero effect in our experiment. Fig. 7b gives a survey of Li diffusivity comparing the current work (black line) with existing literature reports of Li diffusivity in a-Si as a function of the Li composition. The experimental results are indicated by the red symbols (Ding et al., 2009; Simolka et al., 2019; Xie et al., 2010; Yoshimura et al., 2007) and the theoretical modeling by green symbols (Chang et al., 2018; Chou and Hwang, 2013; Johari et al., 2011; Moon et al., 2014; Sivonxay et al., 2020; Wang et al., 2015). There is a vast variation among the literature reports, spanning over 8 orders of magnitude, especially among theoretical models. The variation in the experiments may be partially due to the difference of the material states/properties/defects which are dependent on the synthesis process, and partially by experimental uncertainties. For instance, the diffusivity measurements in amorphous Si using the conventional PITT versus EIS analysis deviated significantly because of various sources of errors such as the unavoidable side reactions at the interface between the electrode and the electrolyte, ambiguity in choosing the diffusion equilibrium potential at a given material composition, the inaccurate measurement of the surface area, material degradation during electrochemical cycles and electrolyte infiltration into a cracked surface (Xie et al., 2010).

4.4. Implication on the battery performance

The deliverable capacity, cyclic efficiency, and rate capability of Li-ion batteries is largely dictated by the Li diffusion kinetics in the electrodes. Although it is expected that the diffusion coefficient of Li in the host is altered when the material composition evolves upon Li reactions, its implication on the battery performance is unclear. Here, we use a simple

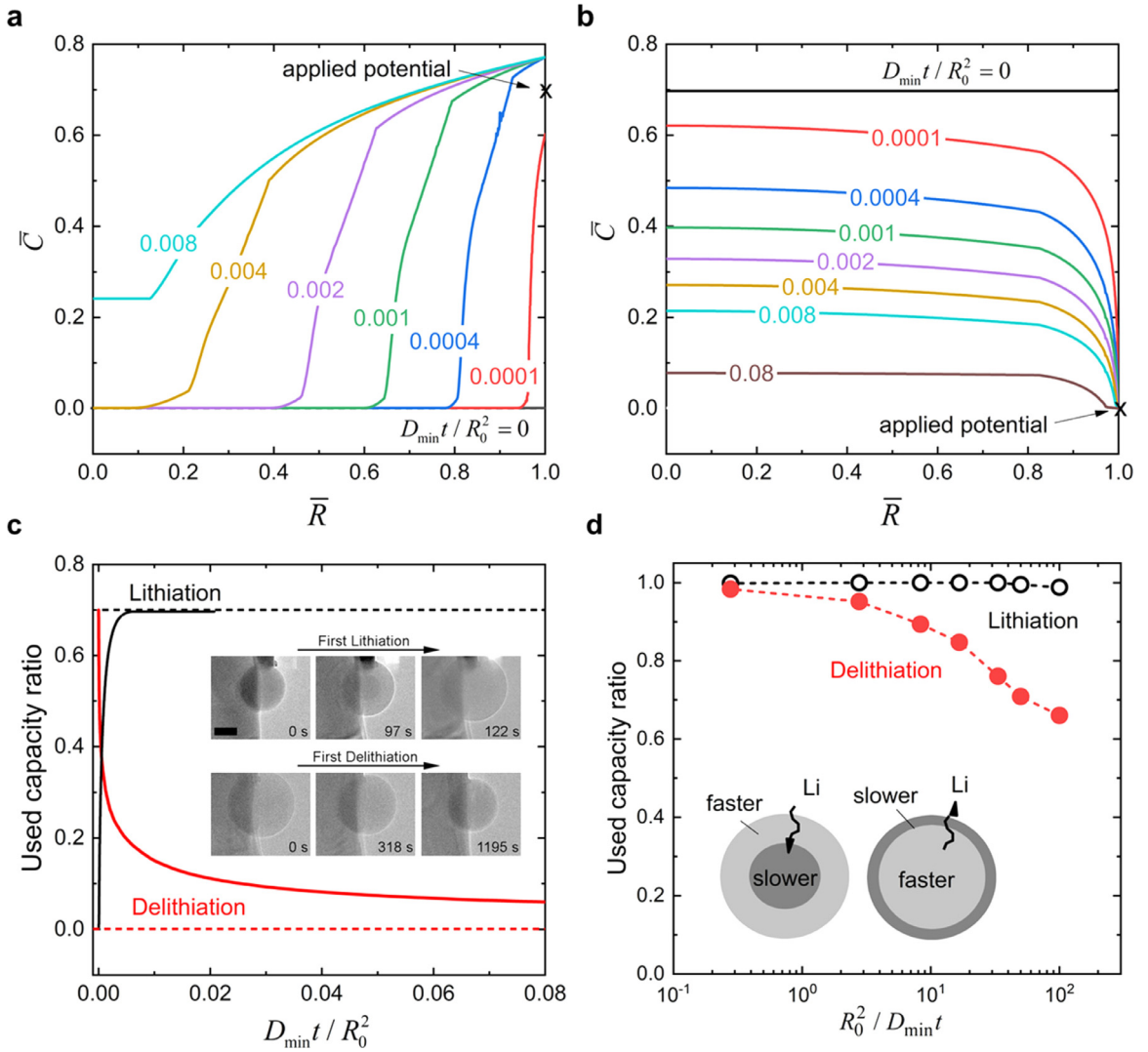

Fig. 8. Impact of the composition-dependent Li diffusivity on the asymmetric rate performance and accessible capacity during lithiation versus delithiation of a Si particle. (a) Propagation of a relatively sharp interface during lithiation of the amorphous Si particle. Different lines show the Li profiles at different normalized times until the completion of Li insertion. (b) Delithiation takes place with a rather smooth concentration gradient profile. (c) The accessible capacity is larger for lithiation than for delithiation of Si. Lithiation takes place at a much higher rate than delithiation. This asymmetric behavior agrees well with the experimental observation (Mcdowell et al., 2013) as shown in the inset of (c). The modeling in (a)-(c) is performed for the particle subject to a constant chemical potential on the outer surface (potentiostatic charging). (d) The asymmetric accessible capacity of Si in lithiation and delithiation at different charging rates when the particle is subject to a constant flux boundary condition (galvanostatic charging).

model of a spherical a-Si particle to illustrate the impact of the composition-dependent Li diffusivity on the asymmetric rate performance, Li trapping, and asymmetric accessible capacity of Si in the lithiation and delithiation cycle.

The Li insertion and extraction are modeled using the diffusion-stress coupled theory described earlier, and the material properties (tracer diffusivity, elastic modulus, yield stress) from the nanoindentation experiments. First, we examine the difference in the Li profiles in the course of lithiation versus delithiation when the Si particle is subject to a constant chemical potential prescribed on its outer surface (potentiostatic charging). Figs. 8a and 8b show the Li distribution along the radial direction at different times of Li insertion and extraction, respectively. The time scale is normalized by the characteristic diffusion time $R_0^2/D_{\min}$ and the radial position is normalized by R_0, where R_0 represents the initial radius of the particle. The dimensionless results are independent on the model size and the computation time. Fig. 8a shows that lithiation of the a-Si particle proceeds through the movement of a relatively sharp concentration gradient. In comparison, delithiation in Fig. 8b shows is a smooth and more homogeneous Li profile over time. This contrast is a consequence of the diffusion coefficient increasing with Li concentration. Similar to the thin film lithiation in the experiments, the steep concentration gradient in the particle lithiation is a result of the lower diffusivity of the pure Si core acting as a bottleneck for Li flux, which leads to the Li accumulation at the lithiation front, Fig. 8a. During delithiation, Li diffusion is faster in the Li-rich inner core than the

Li-depleted outer shell, leading to a relatively homogeneous delithiation of the bulk, Fig. 8b. Supplementary Figure S4 shows the Li profiles in lithiation and delithiation of the Si particle when the stress effect on Li diffusion is not considered. The distinction in the "moving front" versus "smooth Li gradient" behaviors in lithiation/delithiation is more apparent in this case. It is also noted that the Li concentration at the outer surface of the particle ($\bar{R} = 1$) in Fig. 8a is not constant because of the evolving stress field. Supplementary Figure S4 shows the radial distribution of Li concentration, hydrostatic stress, and the diffusion potential at the end of the potentiostatic charging. The mechanical and chemical driving forces complement each other and yield a constant diffusion potential across the radius (dashed line in Figure S4). The distinct lithiation and delithiation behaviors in the a-Si particle corroborates the in-situ TEM observations (McDowell et al., 2013) as reproduced in the inset of Fig. 8c.

Fig. 8c demonstrates another consequence of the faster diffusion at high concentrations, which is that lithiation (black line) completes faster than delithiation (red line) in Si. In fact, during delithiation, even after 10 times longer the time required for full lithiation, there is still over 5% of "trapped" Li inside the particle. This result seems to explain the TEM observation that delithiation is considerably slower than lithiation (bottom versus top rows in the inset panel) and that volume recovery is not accomplished even after long delithiation times. Indeed, Li trapping is now a recognized problem in Si electrodes (Jerliu et al., 2017b; Lindgren et al., 2019). Initially, the accumulated capacity loss in Si electrodes was solely attributed to fracture and solid electrolyte interphase (SEI) reconstruction effects (Chen et al., 2020); however, recent studies have determined that the capacity loss is present even without those effects (Lindgren et al., 2019; Rehnlund et al., 2017; Zhu et al., 2019). A recent study (Zhu et al., 2019) demonstrated that the columbic efficiency of Si electrodes can be improved via isovalent isomorphism which reduces the energy barrier for diffusion and consequently reduces Li trapping. Our findings explain the underlying mechanism behind the Li trapping effect in Si electrodes. Under the condition of potentiostatic charging, the asymmetry in Fig. 8c shows that the accessible capacity of Si upon Li insertion and Li extraction at the same rate is drastically different. To make this comparison more explicit, we perform galvanostatic charging of the Si particle by prescribing a constant Li flux at the particle surface. At the galvanostatic (dis)charging condition, it is easier to extract the electrode capacity at a given rate. Fig. 8d shows the increasing asymmetry of the lithiation and delithiation capacities when the particle is cycled at different rates. The inset sketch illustrates the source of the asymmetry. During Li insertion, the diffusivity is higher in the Li-rich outer shell, enabling a large Li influx and mitigating the rapid saturation of the surface. In comparison, upon Li extraction, the diffusivity is lower in the Li-poor outer shell, limiting the outflux, and consequently, Li is quickly depleted at the outer surface. The phenomena of Li reactions in Si are intricate. Another interesting observation in literature is that the steep concentration gradient at the lithiation front was only clearly observed during the first cycle, while the Li distribution in the following insertion cycles appeared smoother (McDowell et al., 2013; Miao and Thompson, 2018). A plausible explanation for this behavior is that, since Li diffusivity increases substantially with the Li content, if Li is trapped in Si particles after the first delithiation, the lower-bound of diffusivity in the subsequent cycles would be higher than that in the initial cycle which effectively flattens the concentration profile. The prior experimental result (Miao and Thompson, 2018) is in support of this hypothesis that Li trapping is a precursor for the change of behavior from the first to subsequent cycles. In this report (Miao and Thompson, 2018), the diffusivity was found to increase with Li concentration in the first cycle, but was higher and roughly remained constant in the subsequent cycle. Another factor to consider is that the irreversible volume of Si upon Li cycles observed in experiments may be attributed to the creation of the atomic free volume during delithiation (Bower et al., 2015; Li et al., 2020) which could also significantly alter the transport properties.

5. Conclusions

Operando indentation provides an unprecedented capability to measure the real-time evolution of the mechanical properties of redox active materials during the exercise of charging and discharging. This paper demonstrates an inverse use of this experimental platform – we understand the Li reaction kinetics in Li-ion batteries through mechanics-informed chemistry. Nanoindentation experiments are performed to probe the local Li composition throughout the material using the functional dependence of the mechanical properties and material topography on the material composition. The experiment is conducted by instrumented nanoindentation in a controlled inert gas environment, allowing the slow process of diffusion to be probed over the course of several weeks. Results show that Li diffusivity in a-Si increases over three orders of magnitude from the pristine state to the fully lithiated state. This highly composition-dependent diffusivity creates an asymmetry on the rate performance and accessible capacity of batteries during lithiation versus delithiation. Lithiation of a-Si is fast and proceeds via a steep concentration gradient which generates a moving lithiation front between the lithiated and pristine Si, while delithiation is slow and displays a smooth and homogeneous Li profile. The experiments are further understood by theoretical modeling using the material parameters determined by the nanoindentation experiments and the coupled theory of large deformation and diffusion. A quantitative assessment of the stress regulation on Li diffusion is a focused interest of this work. In the model system of the a-Si thin film, the mechanical driving force for Li diffusion due to the hydrostatic stress is less significant than the effect of the solution non-ideality. Models assuming an ideal solution of lithiated Si would drastically overestimate the stress effect on the Li flux and equilibrium concentration. We further design the Li self-redistribution experiments to demonstrate the characteristic of the stress-modulated Li transport in the film. The simple geometry of the a-Si thin film allows us to evaluate the mechanical bias to the chemical potential of Li in a quantitative manner. Overall, this study highlights the need for experimental tools to probe the Li concentration and measure the local

and evolving material properties in the course of Li reactions. It also offers a new understanding of the lithiation kinetics in batteries from the mechanics perspective, and demonstrates the capability of operando nanoindentation in informing the material chemistry and aiding battery research beyond the mechanical measurement.

Declaration of Competing Interest

The authors declare no conflict of interest.

Acknowledgments

The authors are grateful for the support of the National Science Foundation through the grants CMMI-1726392 and DMR-1832707.

Supplementary materials

Supplementary material associated with this article can be found, in the online version, at doi:10.1016/j.jmps.2020.104102.

References

Balke, N., Jesse, S., Morozovska, A.N., Eliseev, E., Chung, D.W., Kim, Y., Adamczyk, L., García, R.E., Dudney, N., Kalinin, S.V., 2010. Nanoscale mapping of ion diffusion in a lithium-ion battery cathode. Nat. Nanotechnol. 5, 749–754.
Balluffi, R.W., Allen, S.M., Carter, W.C., 2005. Kinetics of Materials. John Wiley & Sons.
Bazant, M.Z., 2013. Theory of chemical kinetics and charge transfer based on nonequilibrium thermodynamics. Acc. Chem. Res. 46, 1144–1160.
Beaulieu, L.Y., Eberman, K.W., Turner, R.L., Krause, L.J., Dahna, J.R., 2001. Colossal reversible volume changes in lithium alloys. Electrochem. Solid-State Lett. 4, A137.
Beaulieu, L.Y., Hatchard, T.D., Bonakdarpour, A., Fleischauer, M.D., Dahn, J.R., 2003. Reaction of Li with alloy thin films studied by in situ AFM. J. Electrochem. Soc. 150, A1457.
Berla, L.A., Lee, S.W., Cui, Y., Nix, W.D., 2015. Mechanical behavior of electrochemically lithiated silicon. J. Power Sources 273, 41–51.
Boltzmann, L., 1894. Zur Integration der Diffusionsgleichung bei variabeln Diffusionscoefficienten. Ann. Phys. 289, 959–964.
Bordes, A., De Vito, E., Haon, D., Secouard, C., Montani, A., Marcus, P., 2015. Investigation of lithium insertion mechanisms of a thin-film Si electrode by coupling time-of-flight secondary-ion mass spectrometry, X-ray photoelectron spectroscopy, and focused-ion-beam/SEM. ACS Appl. Mater. Interfaces 7, 27853–27862.
Bower, A.F., Chason, E., Guduru, P.R., Sheldon, B.W., 2015. A continuum model of deformation, transport and irreversible changes in atomic structure in amorphous lithium-silicon electrodes. Acta Mater 98, 229–241.
Bucci, G., Nadimpalli, S.P.V., Sethuraman, V.A., Bower, A.F., Guduru, P.R., 2014. Measurement and modeling of the mechanical and electrochemical response of amorphous Si thin film electrodes during cyclic lithiation. J. Mech. Phys. Solids 62, 276–294.
Cammarata, R.C., 2009. Generalized thermodynamics of surfaces with applications to small solid systems. Solid State Phys 61, 1–75.
Chang, C., Li, X., Xu, Z., 2018. Microstructure- and concentration-dependence of lithium diffusion in the silicon anode: kinetic Monte Carlo simulations and complex network analysis. Appl. Phys. Lett. 113, 121904.
Chen, J., Fan, X., Li, Q., Yang, H., Khoshi, M.R., Xu, Y., Hwang, S., Chen, L., Ji, X., Yang, C., He, H., Wang, Chongmin, Garfunkel, E., Su, D., Borodin, O., Wang, Chunsheng, 2020. Electrolyte design for LiF-rich solid–electrolyte interfaces to enable high-performance microsized alloy anodes for batteries. Nat. Energy 1–12.
Chen, H.Sen, Han, Y., Yang, L., Bao, Y.H., Chen, J., Li, X., Pang, J., Song, W.L., Fang, D.N., 2019. A method for analyzing two-dimensional lithium ion concentration in the nano silicon films. Appl. Phys. Lett. 115, 264102.
Chevrier, V.L., Dahn, J.R., 2009. First principles model of amorphous silicon lithiation. J. Electrochem. Soc. 156, A454.
Chou, C.Y., Hwang, G.S., 2013. Surface effects on the structure and lithium behavior in lithiated silicon: a first principles study. Surf. Sci. 612, 16–23.
Crank, J., 1975. The Mathematics of Diffusion. Oxford university press.
Cubuk, E.D., Kaxiras, E., 2014. Theory of structural transformation in lithiated amorphous silicon. Nano Lett 14, 4065–4070.
Cui, Zhiwei, Gao, F., Cui, Zhihua, Qu, J., 2012. A second nearest-neighbor embedded atom method interatomic potential for Li–Si alloys. J. Power Sources 207, 150–159.
de Vasconcelos, L.S., Xu, R., Zhao, K., 2017. Operando nanoindentation: a new platform to measure the mechanical properties of electrodes during electrochemical reactions. J. Electrochem. Soc. 164, A3840–A3847.
Leo, Di, V., C., Rejovitzky, E., Anand, L., 2015. Diffusion-deformation theory for amorphous silicon anodes: the role of plastic deformation on electrochemical performance. Int. J. Solids Struct. 67–68, 283–296.
Ding, B., Wu, H., Xu, Z., Li, X., Gao, H., 2017. Stress effects on lithiation in silicon. Nano Energy 38, 486–493.
Ding, N., Xu, J., Yao, Y.X., Wegner, G., Fang, X., Chen, C.H., Lieberwirth, I., 2009. Determination of the diffusion coefficient of lithium ions in nano-Si. Solid State Ionics 180, 222–225.
Finegan, D.P., Vamvakeros, A., Cao, L., Tan, C., M Heenan, T.M., Daemi, S.R.M., Jacques, S.D., Beale, A.M., Di Michiel, M., Smith, K.L., Brett, D.J., Shearing, P.R., Ban, C., 2019. Spatially resolving lithiation in silicon–graphite composite electrodes via in situ high-energy X-ray diffraction computed tomography. Nano Lett 19, 3820.
Ghannoum, A., Norris, R.C., Iyer, K., Zdravkova, L., Yu, A., Nieva, P., 2016. Optical characterization of commercial lithiated graphite battery electrodes and in situ fiber optic evanescent wave spectroscopy. ACS Appl. Mater. Interfaces 8, 18763–18769.
Ghassemi, H., Au, M., Chen, N., Heiden, P.A., Yassar, R.S., 2011. In situ electrochemical lithiation/delithiation observation of individual amorphous Si nanorods. ACS Nano 5, 7805–7811.
Harris, S.J., Timmons, A., Baker, D.R., Monroe, C., 2010. Direct in situ measurements of Li transport in Li-ion battery negative electrodes. Chem. Phys. Lett. 485, 265–274.
Harrison, L.G., 1961. Influence of dislocations on diffusion kinetics in solids with particular reference to the alkali halides. Trans. Faraday Soc. 57, 1191–1199.
Hatchard, T.D., Dahn, J.R., 2004. In Situ XRD and Electrochemical Study of the Reaction of Lithium with Amorphous Silicon. J. Electrochem. Soc. 151, A838.
Hay, J., Agee, P., Herbert, E., 2010. Continuous stiffness measurement during instrumented indentation testing. Exp. Tech. 34, 86–94.
Hoffmann, M., Zier, M., Oswald, S., Eckert, J., 2015. Challenges for lithium species identification in complementary Auger and X-ray photoelectron spectroscopy. J. Power Sources 288, 434–440.
Hü, E., Dö, L., Schmidt, H., 2018. Permeation, solubility, diffusion and segregation of lithium in amorphous silicon layers. Chem. Mater 30, 3254–3264.

Jerliu, B., Dörrer, L., Hüger, E., Seidlhofer, B.K., Steitz, R., Borchardt, G., Schmidt, H., 2017a. Electrochemical lithiation of silicon electrodes: neutron reflectometry and secondary ion mass spectrometry investigations. Int. J. Mater. Res. 108, 999–1007.
Jerliu, B., Hüger, E., Horisberger, M., Stahn, J., Schmidt, H., 2017b. Irreversible lithium storage during lithiation of amorphous silicon thin film electrodes studied by in-situ neutron reflectometry. J. Power Sources 359, 415–421.
Johari, P., Qi, Y., Shenoy, V.B., 2011. The mixing mechanism during lithiation of Si negative electrode in Li-ion batteries: an Ab initio molecular dynamics study. Nano Lett 11, 5494–5500.
Kugler, S., Molnr, G., Petö, G., Zsoldos, E., Rosta, L., Menelle, A., Bellissent, R., 1989. Neutron-diffraction study of the structure of evaporated pure amorphous silicon. Phys. Rev. B 40, 8030–8032.
Laforge, B., Levan-Jodin, L., Salot, R., Billard, A., 2008. Study of germanium as electrode in thin-film battery. J. Electrochem. Soc. 155, A181–A188.
Larche, F.C., Cahn, J.I., 1982. The effect of self-stress on diffusion in solids. Acta Metall 30, 1835–1845.
Larché, F.C., Cahn, J.W., 1985. The interactions of composition and stress in crystalline solids. Acta Metall 33, 331–357.
Larché, F.C., Voorhees, P.W., 1996. Diffusion and stresses: basic thermodynamics. Defect Diffus. Forum 129–130, 31–36.
Li, J., Dudney, N.J., Xiao, X., Cheng, Y.T., Liang, C., Verbrugge, M.W., 2015. Asymmetric rate behavior of Si anodes for lithium-ion batteries: ultrafast de-lithiation versus sluggish lithiation at high current densities. Adv. Energy Mater. 5, 1–6.
Li, J., Xiao, X., Yang, F., Verbrugge, M.W., Cheng, Y.T., 2012. Potentiostatic intermittent titration technique for electrodes governed by diffusion and interfacial reaction. J. Phys. Chem. C 116, 1472–1478.
Li, J.Y., Xu, Q., Li, G., Yin, Y.X., Wan, L.J., Guo, Y.G., 2017. Research progress regarding Si-based anode materials towards practical application in high energy density Li-ion batteries. Mater. Chem. Front. 1, 1691–1708.
Li, Y., Mao, W., Zhang, Q., Zhang, K., Yang, F., 2020. A free volume-based viscoplastic model for amorphous silicon electrode of lithium-ion battery. J. Electrochem. Soc. 167, 040518.
Lim, J., Li, Y., Alsem, D.H., So, H., Lee, S.C., Bai, P., Cogswell, D.A., Liu, X., Jin, N., Yu, Y.S., Salmon, N.J., Shapiro, D.A., Bazant, M.Z., Tyliszczak, T., Chueh, W.C., 2016. Origin and hysteresis of lithium compositional spatiodynamics within battery primary particles. Science 353, 566–571.
Lindgren, F., Rehnlund, D., Pan, R., Pettersson, J., Younesi, R., Xu, C., Gustafsson, T., Edström, K., Nyholm, L., 2019. On the capacity losses seen for optimized nano-Si composite electrodes in Li-metal half-cells. Adv. Energy Mater. 9, 1901608.
Lubliner, J., 2008. Plasticity Theory. Courier Corporation.
McDowell, M.T., Lee, S.W., Harris, J.T., Korgel, B.A., Wang, C., Nix, W.D., Cui, Y., 2013. In situ TEM of two-phase lithiation of amorphous silicon nanospheres. Nano Lett 13, 758–764.
McDowell, M.T., Ryu, I., Lee, S.W., Wang, C., Nix, W.D., Cui, Y., 2012. Studying the kinetics of crystalline silicon nanoparticle lithiation with in situ transmission electron microscopy. Adv. Mater. 24, 6034–6041.
Mehrer, H., 1996. The effect of pressure on diffusion. Defect Diffus. Forum 129–130, 57–76.
Miao, J., Thompson, C.V., 2018. Kinetic study of the initial lithiation of amorphous silicon thin film anodes. J. Electrochem. Soc. 165, A650–A656.
Michael, A., Kwok, C.Y., Wang, P., Kazuo, O., Varlamov, S., 2015. Investigation of E-beam evaporated silicon film properties for MEMS applications. J. Microelectromechanical Syst. 24, 1951–1959.
Mims, C., 2018. The battery boost we've been waiting for is only a few years out. Wall Str. J. 1–5.
Mitra, S., Stark, J.P., Tatti, S.R., 1991. On the use of the Boltzmann-Matano analysis to deduce concentration-dependent diffusivity. J. Phys. Chem. Solids 52, 463–465.
Moon, J., Lee, B., Cho, M., Cho, K., 2014. Ab initio and kinetic Monte Carlo simulation study of lithiation in crystalline and amorphous silicon. J. Power Sources 272, 1010–1017.
Mu, L., Zhang, R., Kan, W.H., Zhang, Y., Li, L., Kuai, C., Zydlewski, B., Rahman, M.M., Sun, C.J., Sainio, S., Avdeev, M., Nordlund, D., Xin, H.L., Lin, F., 2019. Dopant Distribution in Co-Free High-Energy Layered Cathode Materials. Chem. Mater. 31, 9769–9776.
Nadimpalli, S.P.V., Sethuraman, V.A., Bucci, G., Srinivasan, V., Bower, A.F., Guduru, P.R., 2013. On plastic deformation and fracture in Si films during electrochemical lithiation/delithiation cycling. J. Electrochem. Soc. 160, A1885–A1893.
Okugawa, M., Numakura, H., 2015. Discussion of "On the Boltzmann–Matano analysis of diffusion in a semi-infinite medium." Metall. Mater. Trans. A Phys. Metall. Mater. Sci. 46, 3813–3814.
Oliver, W.C., Pharr, G.M., 2004. Measurement of hardness and elastic modulus by instrumented indentation: advances in understanding and refinements to methodology. J. Mater. Res. 19, 3–20.
Pan, J., Zhang, Q., Li, J., Beck, M.J., Xiao, X., Cheng, Y.-T., 2015. Effects of stress on lithium transport in amorphous silicon electrodes for lithium-ion batteries. Nano Energy 13, 192–199.
Pharr, G.M., Oliver, W.C., Brotzen, F.R., 1992. On the generality of the relationship among contact stiffness, contact area, and elastic modulus during indentation. J. Mater. Res. 7, 613–617.
Pharr, M., Suo, Z., Vlassak, J.J., 2013. Measurements of the fracture energy of lithiated silicon electrodes of Li-Ion batteries. Nano Lett 13, 5570–5577.
Philibert, J., 1996. Diffusion and stresses. Defect Diffus. Forum 129–130, 3–8.
Pietsch, P., Hess, M., Ludwig, W., Eller, J., Wood, V., 2016. Combining operando synchrotron X-ray tomographic microscopy and scanning X-ray diffraction to study lithium ion batteries. Sci. Rep. 6, 27994.
Poirier, D.R., Geiger, G.H., 2018. Transport Phenomena in Materials Processing. Springer.
Radvanyi, E., De Vito, E., Porcher, W., Danet, J., Desbois, P., Colin, J.F., Si Larbi, S.J., 2013. Study of lithiation mechanisms in silicon electrodes by Auger Electron Spectroscopy. J. Mater. Chem. A 1, 4956–4965.
Rehnlund, D., Lindgren, F., Böhme, S., Nordh, T., Zou, Y., Pettersson, J., Bexell, U., Boman, M., Edström, K., Nyholm, L., 2017. Lithium trapping in alloy forming electrodes and current collectors for lithium based batteries. Energy Environ. Sci. 10, 1350–1357.
Sethuraman, V.A., Chon, M.J., Shimshak, M., Srinivasan, V., Guduru, P.R., 2010. In situ measurements of stress evolution in silicon thin films during electrochemical lithiation and delithiation. J. Power Sources 195, 5062–5066.
Sharma, N., Peterson, V.K., Elcombe, M.M., Avdeev, M., Studer, A.J., Blagojevic, N., Yusoff, R., Kamarulzaman, N., 2010. Structural changes in a commercial lithium-ion battery during electrochemical cycling: an in situ neutron diffraction study. J. Power Sources 195, 8258–8266.
Sheldon, B.W., Soni, S.K., Xiao, X., Qi, Y., 2012. Stress contributions to solution thermodynamics in Li-Si alloys. Electrochem. Solid-State Lett. 15.
Simolka, M., Heim, C., Friedrich, K.A., Hiesgen, R., 2019. Visualization of local ionic concentration and diffusion constants using a tailored electrochemical strain microscopy method. J. Electrochem. Soc. 166, A5496–A5502.
Sivonxay, E., Aykol, M., Persson, K.A., 2020. The lithiation process and Li diffusion in amorphous SiO_2 and Si from first-principles. Electrochim. Acta 331, 135344.
Tabor, D., 2000. The Hardness of Metals. Clarendon Press.
Tripuraneni, R., Rakshit, S., Nadimpalli, S.P.V., 2018. In situ measurement of the effect of stress on the chemical diffusion coefficient of Li in high-energy–density electrodes. J. Electrochem. Soc. 165, A2194–A2202.
Tsui, T.Y., Pharr, G.M., 1999. Substrate effects on nanoindentation mechanical property measurement of soft films on hard substrates. J. Mater. Res. 14, 292–301.
Verbrugge, M.W., Koch, B.J., 1996. Modeling lithium intercalation of single-fiber carbon microelectrodes. J. Electrochem. Soc. 143, 600.
Wang, F., Graetz, J., Moreno, M.S., Ma, C., Wu, L., Volkov, V., Zhu, Y., 2011. Chemical distribution and bonding of lithium in intercalated graphite: identification with optimized electron energy loss spectroscopy. ACS Nano 5, 1190–1197.
Wang, J.W., He, Y., Fan, F., Liu, X.H., Xia, S., Liu, Y., Harris, C.T., Li, H., Huang, J.Y., Mao, S.X., Zhu, T., 2013. Two-phase electrochemical lithiation in amorphous silicon. Nano Lett 13, 709–715.

Wang, X., Singh, S.S., Ma, T., Lv, C., Chawla, N., Jiang, H., 2017. Quantifying electrochemical reactions and properties of amorphous silicon in a conventional lithium-ion battery configuration. Chem. Mater. 29, 5831–5840.
Wang, Z., Su, Q., Deng, H., Fu, Y., 2015. Composition dependence of lithium diffusion in lithium silicide: a density functional theory study. ChemElectroChem 2, 1292–1297.
Wohl, K., 1946. Thermodynamic evaluation of binary and ternary liquid systems. Trans. Am. Inst. Chem. Eng. 42, 215–249.
Wolf, M., May, B.M., Cabana, J., 2017. Visualization of electrochemical reactions in battery materials with X-ray microscopy and mapping. Chem. Mater. 29, 3347–3362.
Wu, Y., Liu, N., 2018. Visualizing battery reactions and processes by using in situ and in operando microscopies. Chem 4, 438–465.
Xie, J., Imanishi, N., Zhang, T., Hirano, A., Takeda, Y., Yamamoto, O., 2010. Li-ion diffusion in amorphous Si films prepared by RF magnetron sputtering: a comparison of using liquid and polymer electrolytes. Mater. Chem. Phys. 120, 421–425.
Xu, R., de Vasconcelos, L.S., Shi, J., Li, J., Zhao, K., 2018. Disintegration of meatball electrodes for $LiNi_xMn_yCo_zO_2$ cathode materials. Exp. Mech. 58, 549–559.
Xu, R., de Vasconcelos, L., Zhao, K., 2016. Computational analysis of chemomechanical behaviors of composite electrodes in Li-ion batteries. J. Mater. Res. 31, 2715–2727.
Xu, R., Zhao, K., 2018. Corrosive fracture of electrodes in Li-ion batteries. J. Mech. Phys. Solids 121, 258–280.
Xu, R., Yang, Y., Yin, F., Liu, P., Cloetens, P., Liu, Y., Lin, F., Zhao, K., 2019. Heterogeneous damage in Li-ion batteries: Experimental analysis and theoretical modeling. J. Mech. Phys. Solids 129, 160–183.
Xu, R., Zhao, K., 2016. Mechanical interactions regulated kinetics and morphology of composite electrodes in Li-ion batteries. Extrem. Mech. Lett. 8, 13–21.
Yang, Y., Xu, R., Zhang, K., Lee, S., Mu, L., Liu, P., Waters, C.K., Spence, S., Xu, Z., Wei, C., Kautz, D.J., Yuan, Q., Dong, Y., Yu, Y., Xiao, X., Lee, H., Pianetta, P., Cloetens, P., Lee, J., Zhao, K., Lin, F., Liu, Y., 2019. Quantification of heterogeneous degradation in Li-ion batteries. Adv. Energy Mater. 9, 1900674.
Yoon, I., Abraham, D.P., Lucht, B.L., Bower, A.F., Guduru, P.R., 2016. In situ measurement of solid electrolyte interphase evolution on silicon anodes using atomic force microscopy. Adv. Energy Mater. 6, 1600099.
Yoshimura, K., Suzuki, J., Sekine, K., Takamura, T., 2007. Measurement of the diffusion rate of Li in silicon by the use of bipolar cells. J. Power Sources 174, 653–657.
Yu, W.J., Liu, C., Hou, P.X., Zhang, L., Shan, X.Y., Li, F., Cheng, H.M., 2015. Lithiation of silicon nanoparticles confined in carbon nanotubes. ACS Nano 9, 5063–5071.
Zhang, H.W., Subhash, G., Jing, X.N., Kecskes, L.J., Dowding, R.J., 2006. Evaluation of hardness-yield strength relationships for bulk metallic glasses. Philos. Mag. Lett. 86, 333–345.
Zhang, Y., Fincher, C., McProuty, S., Pharr, M., 2019. In-operando imaging of polysulfide catholytes for Li–S batteries and implications for kinetics and mechanical stability. J. Power Sources 434, 226727.
Zhao, K., Pharr, M., Cai, S., Vlassak, J.J., Suo, Z., 2011a. Large plastic deformation in high-capacity lithium-ion batteries caused by charge and discharge. J. Am. Ceram. Soc. 94, 226–235.
Zhao, K., Pharr, M., Vlassak, J.J., Suo, Z., 2011b. Inelastic hosts as electrodes for high-capacity lithium-ion batteries. J. Appl. Phys. 109, 016110.
Zhao, K., Tritsaris, G.A., Pharr, M., Wang, W.L., Okeke, O., Suo, Z., Vlassak, J.J., Kaxiras, E., 2012. Reactive flow in silicon electrodes assisted by the insertion of lithium. Nano Lett 12, 4397–4403.
Zhu, B., Liu, G., Lv, G., Mu, Y., Zhao, Y., Wang, Y., Li, X., Yao, P., Deng, Y., Cui, Y., Zhu, J., 2019. Minimized lithium trapping by isovalent isomorphism for high initial Coulombic efficiency of silicon anodes. Sci. Adv. 5 eaax0651.